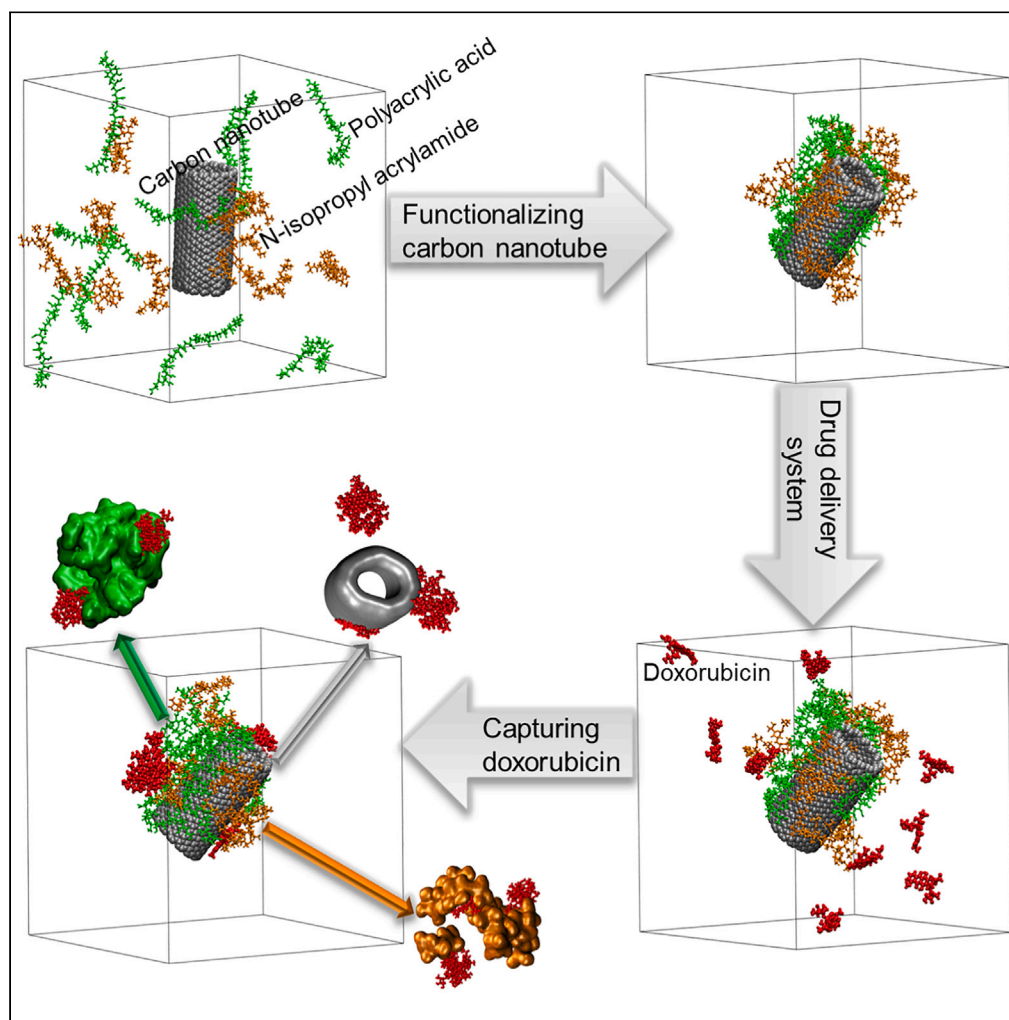**Article**

Molecular dynamics investigation on synthesis of a pH- and temperature-sensitive carbon nanotube loaded with doxorubicin

Qijiang Shu,
Pengru Huang, Zhi
Dong, Wenping
Wang

14787485422@163.com (Q.S.)
wangwenping@ynutcm.edu.cn
(W.W.)

Highlights

Drug delivery system takes
into account light,
temperature, and pH
excitation factors

All functional molecules are
adhered to the carbon
nanotube wall

Functionalized carbon
nanotube captures all
dispersed doxorubicin
molecules

Formation kinetics and
drug loading mechanism of
multifunctional carbon
nanotube

Article

Molecular dynamics investigation on synthesis of a pH- and temperature-sensitive carbon nanotube loaded with doxorubicin

Qijiang Shu,[1,3,4,6,*] Pengru Huang,[5] Zhi Dong,[2] and Wenping Wang[2,*]

SUMMARY

The many exotic properties of carbon nanotubes (CNTs) make them a powerful attraction in the field of drug delivery systems (DDS). In this work, based on quantum chemical calculation and molecular simulation techniques, polyacrylic acid (PAA) and N-isopropyl acrylamide (NIP) are selected and acted simultaneously on the CNT to form a stable system (FCNT). As a potential DDS, FCNT captures the dispersed doxorubicin (DOX) molecules around it and maintains a stable configuration. In these processes, electrostatic and van der Waals forces act synergistically, with van der Waals forces dominating. Compared to NIP, PAA molecules exhibit stronger adhesion and encapsulation efficiency to CNT and stronger adsorption capacity to DOX. This study reveals the mechanism of action among PAA, NIP, CNT, and DOX, providing feasibility verification and prospective guidance for the experimental synthesis of PAA-NIP-CNT-type multifunctional DDS, and also broadening the idea for exploring more efficient DDS suitable for DOX.

INTRODUCTION

Cancer is a major threat to human health in the world, and targeted drug delivery is one of the important options for cancer treatment.[1–3] Doxorubicin (DOX), the most common chemotherapy drug in the anthracycline family, is widely used to treat different types of cancer. However, DOX destroys the molecular structure of cancer cells and inhibits their growth while also destroying healthy cells near the tumor.[4,5] In current drug development, nearly 40% of marketed drugs and 90% of candidate drugs have shown poor water solubility, low dissolution, and toxic and side effects similar to DOX, severely limiting their bioavailability. Scientists all over the world are trying to formulate anticancer drugs with different drug delivery systems (DDS), such as liposomes, microemulsions, hydrogels, polymer micelles, lipid-polymer hybridized nanoparticles, etc., to solve the adverse physiological characteristics of drugs and enhance the therapeutic effectiveness of drugs.[6]

In recent years, carbon nanotubes (CNTs) have generated strong appeal in the field of targeted drug delivery.[7–9] The high fluidity and permeability due to the size and shape characteristics of CNTs make them suitable matrices for carrying drugs, proteins, and vaccines. The surface charge and surface chemistry of CNTs provide a relatively isolated environment in which drugs can be loaded on their surface or inside, thus preventing degradation.[10,11] CNT can deliver low-dose drugs on demand with minimal side effects. Another unique advantage of CNT lies in its semiconductor properties, which enable it to act as a bomb under laser irradiation, releasing drugs and destroying cancer cells.[12] A considerable amount of research has shown that CNT is a promising carrier for DOX, as the aromatic rings of DOX can be adsorbed onto CNT through π-π interactions.[13–15]

One problem with CNT in bioenvironmental applications is its insolubility. Due to van der Waals and hydrophobic interactions, CNT particles adhere together in the aqueous environment, which hinders their uniform dispersion throughout the entire blood environment, leading to adverse toxicity. Moreover, the carrier size may become larger due to adhesion and aggregation, making it impossible to penetrate cells for drug delivery.[16] A solution that has rapidly become a research hotspot is to hybridize CNTs with other suitable matrices, which not only improves the biocompatibility of CNTs but also has the potential to achieve organic integration of different drug-carrying endowments to enhance the targeting ability of DDS.[17–20] Some typical reports include increasing the water solubility of CNTs by combining them with highly hydrophilic polymers,[21,22] coupling CNTs with temperature-sensitive polymers to synthesize DDS for drug release under light radiation and temperature changes,[23,24] and incorporating CNTs with pH-sensitive polymers to achieve drug release from DDS in response to light radiation and pH alteration.[25,26] Poly N-isopropyl acrylamide (NIP) is the most appropriate type of temperature-sensitive polymer for reasons that

[1]Institute of Information, Yunnan University of Chinese Medicine, Kunming, Yunnan 650500, China
[2]College of Chinese Materia Medica, Yunnan University of Chinese Medicine, Kunming, Yunnan 650500, China
[3]Yunnan Key Laboratory of Southern Medicinal Utilization, Yunnan University of Chinese Medicine, Kunming, Yunnan 650500, China
[4]Yunnan Traditional Chinese Medicine Prevention and Treatment Engineering Research Center, Yunnan University of Chinese Medicine, Kunming, Yunnan 650500, China
[5]Guangxi Key Laboratory of Information Materials and Guangxi Collaborative Innovation Center of Structure and Property for New Energy and Materials, School of Material Science & Engineering, Guilin University of Electronic Technology, Guilin, Guangxi 541004, China
[6]Lead contact
*Correspondence: 14787485422@163.com (Q.S.), wangwenping@ynutcm.edu.cn (W.W.)
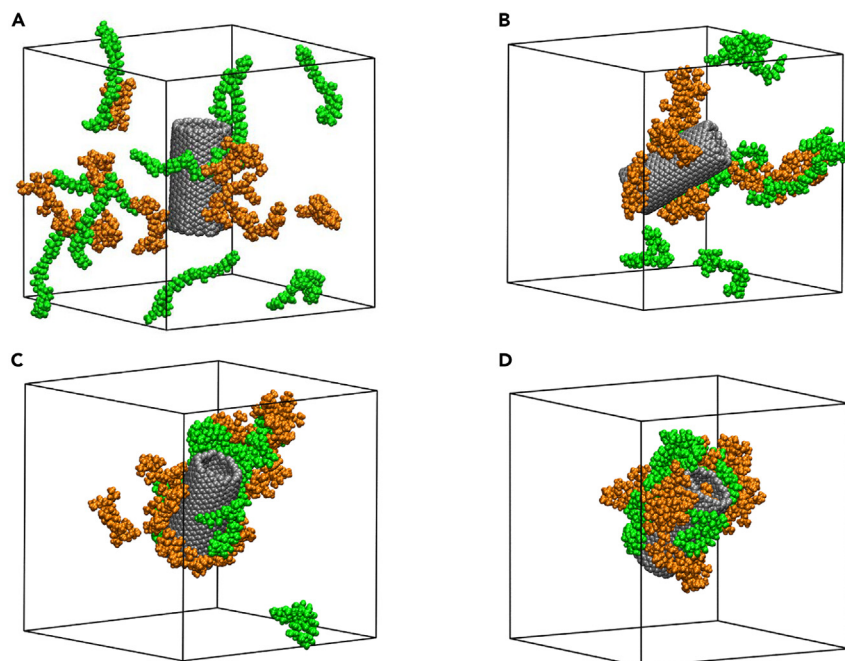https://doi.org/10.1016/j.isci.2024.108812

Figure 1. Snapshots are taken during the 60 ns simulation process for functionalizing CNT by using PAAs and NIPs

(A–D) (A) 0 ns, (B) 20 ns, (C) 40 ns, and (D) 60 ns. CNT (gray), PAAs (green), and NIPs (orange). For clarity, water and virtual sites are not shown. See also Figure S1.

include its critical solubility temperature close to body temperature, the similarity to body network and tissues, and the ability to simultaneously load hydrophilic and hydrophobic compounds, etc.[27] Correspondingly, polyacrylic acid (PAA) is an excellent material for making pH-responsive DDSs because it offers significant advantages over other polymers due to its low toxicity, antigenicity, immunogenicity, and its degree of ionization depends on the pH of the solution.[28] They are the most widely reported "star" polymers.[29,30] However, according to our literature review, the simultaneous application of NIP and PAA to functionalize CNTs and use them for the delivery of DOX has not been reported so far.

Molecular dynamics (MD) simulation is a powerful technique for providing qualitative and quantitative data on the interactions and physicochemical mechanisms of drug systems and has been successfully applied to the study of a large number of DDSs. In this paper, we use NIP and PAA jointly for the first time to modify the CNT surface to fabricate multifunctional DDS integrating light radiation sensitivity, temperature sensitivity, and pH sensitivity. From the perspective of the physiological characteristics of certain parts of the tumor where the temperature is higher than that of the human body and the pH value in the tumor tissue changes from neutral to acidic, such DDS is highly attractive because it not only utilizes CNT to increase drug circulation time and drug accumulation at the tumor site, but also takes into account the three triggering factors of light radiation, temperature, and pH that release drugs at the target site, which will greatly enhance the drug targeting ability. Subsequently, such DDS is used for the study of delivering DOX. The aforementioned processes are based on the MD approach, which not only greatly reduces the experimental cost, but more importantly, makes the mechanism of action of these procedures clear and transparent from the molecular scale. Our work both explores new avenues in the field of smart, novel DDS and lays the groundwork for mining efficient DDS adapted to DOX.

RESULTS AND DISCUSSION

All polymer molecules aggregate toward the CNT, with individual molecules entering the CNT cavity

Ten 10-mer PAA molecular chains and ten 20-mer NIP molecular chains that completed the structural optimization are randomly dispersed in the simulation box, and they are used to functionalize the CNT located at the center of the box, with a simulation time of 60 ns. Figure 1 shows the snapshots of some representative moments during the simulation process. As shown in Figure 1A, at the beginning of the simulation, the CNT represented by gray is at the center of the simulation box, while the PAA molecules denoted in green, and the NIP molecules denoted in orange are randomly dispersed at various positions in the simulation box. With the increase of simulation time, these molecules, which are originally in a dispersed state, gradually aggregate, and as can be seen in Figures 1B–1D, this agglomeration behavior is carried out centered on the CNT. Intuitively, the CNT does not display significant positional translation during the simulation but rather exhibits varying degrees of rotation. The polymer molecules fully aggregate around the CNT at 60 ns (Figure 1D) and exhibit good integrity. In addition, during the simulation, a detail is that only one NIP molecule enters the CNT cavity and remains inside the cavity without escaping, as can be seen from Figures 1D and S1.
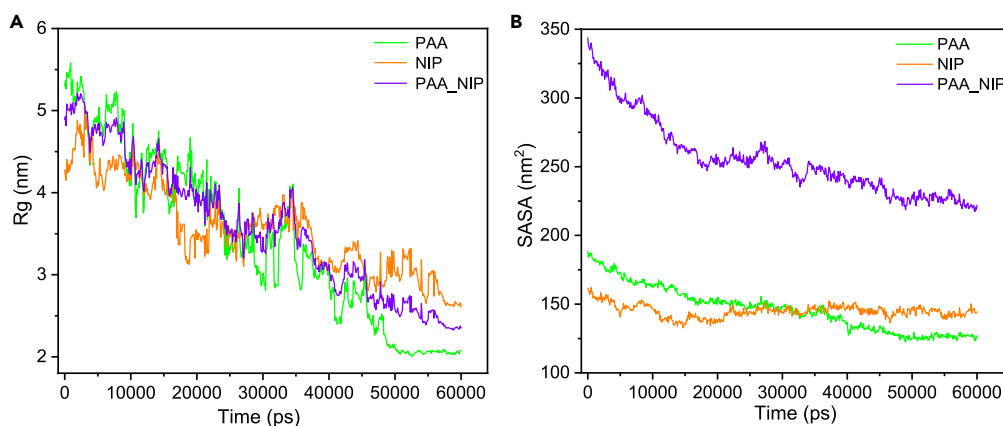
Figure 2. Gyration radius and SASAs of molecular systems
(A and B) Gyration radius (A) and SASAs (B) of groups PAA (green), NIP (orange), and PAA_NIP (purple) over a 60 ns simulation for functionalizing CNT with PAAs and NIPs.

The compactness of polymer molecular systems increases significantly with simulation time and then stabilizes

To further characterize the spatial ductility and compactness of polymer molecules during the functionalization of CNT, the gyration radii[31] and solvent-accessible surface areas (SASA)[32] of PAA, NIP, and PAA-NIP systems are calculated, respectively. As shown in Figure 2A, although the gyration radius of the PAA system (green curve) fluctuates over a small time range, the overall tendency is to decrease rapidly and to maintain a relatively constant value during the last 10 ns of time, suggesting that the PAA molecules aggregate rapidly, and finally maintains the overall conformation unchanged. The gyration radius (orange curve) of the NIP system exhibits a similar rapid decrease in the first 20 ns time range compared to PAA, but decreases relatively slowly in subsequent times, indicating that the conformational change of the NIP system is relatively small in the latter half of the period. Correspondingly, the purple curve in the figure represents the configuration changes when PAA and NIP are considered as a system.

Figure 2B illustrates the SASAs of the polymer molecules system during the simulation. Similar to the trend of gyration radius, the SASA value of PAA gradually decreases after the beginning of the simulation and maintains at a low level in the last 10 ns, while the SASA value of the NIP system decreases significantly in the first 20 ns, and then changes more gently in the following 40 ns. The decrease in the SASA values is strong evidence of the shift of the molecules from dispersion to agglomeration, and this change coincides with the conclusions about the conformational evolution of the molecular system obtained from Figure 2A. The aggregation of the structure of molecular surfactants in solution prevents their contact with water molecules, and this unfavorable interaction between hydrophobic groups and water is one of the powerful forces for the self-assembly of polymer micelles in aqueous solution. The change in the value of SASA illustrated in Figure 2B exemplifies the change in this unfavorable interaction during the agglomeration of polymer molecules.

Polymer molecules mainly adhere to the outer wall of CNT, with PAA molecules exhibiting higher encapsulation efficiency and adhesion compared to NIP molecules

In this work, all PAA molecular chains are numbered from 1 to 10 and the same is done for NIP molecular chains. Figure 3A demonstrates the variation of the distance from the center of mass of each PAA molecule to the center of mass of CNT over simulation time. Although there are individual molecules (e.g., PAA7) that exhibit large fluctuations in their values, these distances all decrease significantly with time and remain nearly constant over the last 10 ns of time. In Figure 3B, the distance between the centroids of NIP3, NIP5, and NIP7 and the CNT centroid decreases slowly over time, while the value of NIP8 fluctuates greatly. At about 12 ns, NIP4 shows an extremely small distance from the CNT compared to the other molecules, and such spacing varies less in subsequent simulations, implying that NIP4 enters the CNT cavity and stays inside the cavity without escaping, which supports the results of Figures 1 and S1. These features make the trend of an overall consistent decrease in NIP molecules not as pronounced as that of PAA molecules. In addition, by comparing Figures 3A and 3B, the typical values of the distance between PAA molecules and CNT at the end of the simulation (60 ns) are 1.4 nm–3.5 nm, while the corresponding values for NIP molecules are 0.7 nm–4.4 nm. The wider range of the latter means that NIP molecules have relatively large dispersion, which can be intuitively seen from the comparison of screenshots of the PAA-CNT system (inset a_0) and NIP-CNT system (inset b_0) at 60 ns.

Figure 4A reveals the number of contacts[33] between different molecules in the simulated system as a function of time, and they are calculated using the following equation:

$$N_C(t) = \sum_{i=1}^{N_A} \sum_{j=1}^{N_B} \int_{r_i}^{r_i+0.6\ nm} \delta(r(t) - r_j(t)) dr \qquad \text{(Equation 1)}$$
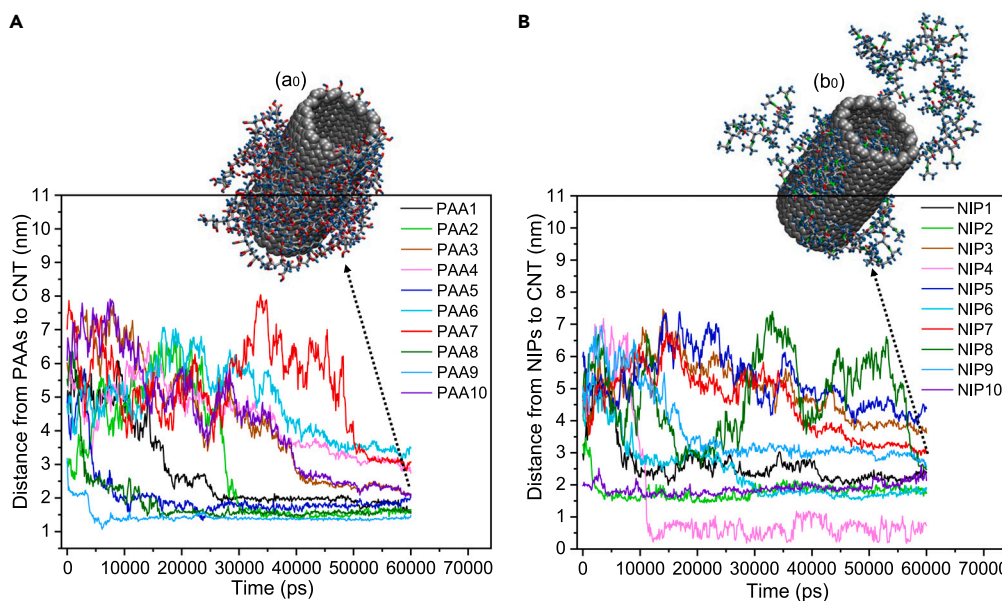
Figure 3. The distance distribution between polymer molecules and CNT

(A and B) (A) Distance from the center of mass of each PAA chain (numbered 1 to 10) in the system to the center of mass of the CNT as a function of simulation time during the process for functionalizing CNT, with a snapshot of the relative position of each PAA chain to the CNT at 60 ns shown in illustration (a_0). Similarly, the corresponding change processes of the NIP chains in the system are shown in figures (B) and (b_0).

where N_A and N_B are the total number of atoms in the A and B molecular groups, r_i is the distance from the jth atom in the B group to the ith atom in the A group. As shown in the figure, the number of contacts between PAA and water molecules (PAA-SOL) decreases rapidly after the beginning of the simulation, the same trend is also reflected in the NIP (NIP-SOL) and CNT (CNT-SOL). Meanwhile, PAA-CNT, NIP-CNT, and PAA-NIP show a slow increase, which coincides with the evolution of PAA, NIP, and CNT from randomly dispersed in the solvent to coalescing into a whole interacting with each other. More precisely, the rise of PAA-CNT as well as NIP-CNT verifies the gradual covering of CNT by PAA and NIP molecules to form a stable envelope, where the smaller increase of NIP-CNT relative to PAA-CNT confirms a relatively weak coverage of CNT by NIP molecules (consistent with the results shown in Figure 3b_0).

To further understand the distribution of molecules around CNT, the radial distribution functions (RDF) of different molecular systems are calculated using the following equation[34]:

$$g_{CNT-A}(r) = \frac{\langle \rho_A(r) \rangle}{\langle \rho_A \rangle_{local}} \frac{1}{\langle \rho_A \rangle_{local}} \frac{1}{N_{CNT}} \int\limits_{i \in CNT}^{N_{CNT}} \int\limits_{j \in A}^{N_A} \frac{\delta(r_{ij} - r)}{4\pi r^2} \qquad \text{(Equation 2)}$$

where $\langle \rho_A(r) \rangle$ is the partial density of component A at a distance r from CNT, and $\langle \rho_A \rangle_{local}$ is the average partial density of the A component in a sphere of radius r around CNT. Figure 4B shows the calculation results, where the horizontal axis represents the distance r and the vertical axis corresponds to the RDF. The RDF curve has two peaks in the approximate range of 0.5 nm–2.5 nm, with one of the largest peaks present near 0.62 nm, which is the main distance at which the interaction between the polymer molecule and the CNT occurs. Compared to the CNT-PAA system, the maximum peak of the CNT-NIP system is lower and the center peak shifts toward the direction of increasing distance, indicating that the encapsulation efficiency of NIP on CNT is lower and the adhesion between them is relatively weak, which is validated with the conclusion in Figure 4A.

The van der Waals interaction is the main driving force for the adsorption of polymer molecules on the surface of CNT to form stable envelopes

Figure 5A demonstrates the variation of the number of hydrogen bonds[35,36] between different molecules in the system with simulation time. The number of hydrogen bonds between PAA and water molecules (PAA-SOL) rapidly decreases, while the number of hydrogen bonds between PAA and PAA (PAA-PAA), as well as between PAA and NIP (PAA-NIP), increases accordingly. Similar trends also apply to NIP, but their magnitude of change is smaller than that of PAA. The trend in the number of hydrogen bonds is consistent with the change in the number of intermolecular contacts (Figure 4A), suggesting that hydrogen bonding plays an important role in the evolution of polymer molecules from dispersion to aggregation.

Figure 5B depicts the van der Waals interaction energy (Vdw) and electrostatic interaction energy (Elec.) between molecules in the system. Negative value indicates attraction energy and positive value represents repulsion energy. As shown, the decrease in Elec. and Vdw of
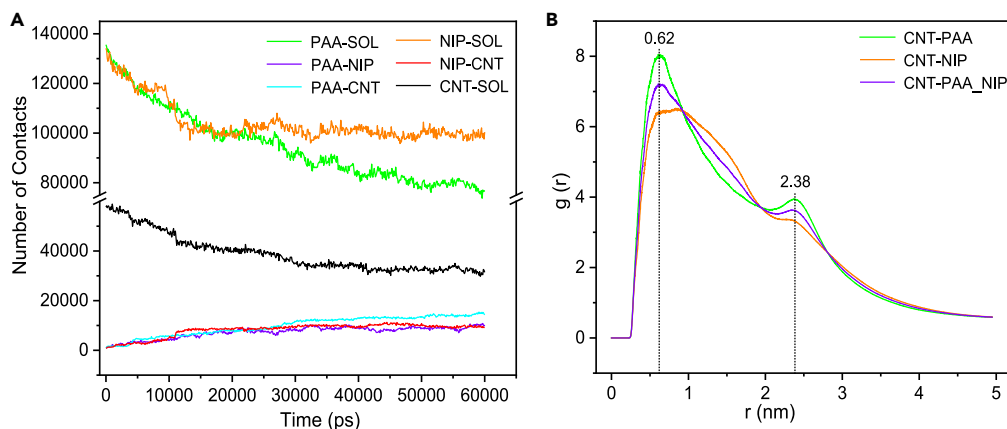
Figure 4. Intermolecular contact and their radial distribution
(A) Variation of the number of atomic contacts between different groups of molecules with simulation time during the functionalization of CNT.
(B) RDF of different groups of molecules around the CNT during the simulation.

PAA-PAA with simulation time suggests that electrostatic interactions and van der Waals interactions are important driving forces for the aggregation of PAA molecules, with the greater magnitude of the change in Elec. proving the dominance of electrostatic interactions. Correspondingly, the changes in Elec. and Vdw of NIP-NIP are relatively small, with Elec. being positive, indicating that electrostatic interactions between NIP molecules exhibit repulsive forces, while the negative values of Vdw reflect the van der Waals attraction between molecules, which suggests that the aggregation process of NIP is accompanied by the synergistic effect of these two forces. More precisely, the process of molecular aggregation described previously also involves interactions between different classes of molecules, as evidenced by the apparent change in the Elec. and Vdw curves of PAA-NIP in the figure. In addition, the significant decrease in the Vdw values of PAA-CNT and NIP-CNT indicates that van der Waals interaction is the main driving force for polymer molecules to be adsorbed on the CNT surface to form stable envelopes. The larger variation in Vdw of PAA-CNT indicates stronger adhesion between PAA molecules and the CNT surface, which is consistent with the conclusions elaborated in the previous section.

The functionalized CNT captures all doxorubicin molecules dispersed around it, demonstrating good drug-loading properties

The CNT functionalized by PAA and NIP molecules (FCNT) is used as DDS and placed in the center of the simulation box, and ten DOX molecules are randomly inserted into the simulation box, simulating 80 ns. Figure 6 illustrates the process of FCNT capturing the target drug DOX. Figure 6A shows the initial state of the simulation system. With the prolongation of the simulation time, the DOX molecules gradually aggregate with FCNT as the center and eventually adhere to the surface of FCNT. The entire system exhibits a stable nano-drug-carrier morphology, as shown in Figures 6B–6E.

To quantitatively characterize the positional relationship between the drug and the FCNT, the ten DOX molecules in the simulation box are numbered individually (DOX1–DOX10), and the distances between their centers of mass and the CNT over time are counted and displayed in Figure 7. As shown in Figure 7, the distances of individual DOX molecules from the CNT show relatively large fluctuating changes in the time range of about 0–30 ns, but the overall trend is rapidly decreasing, with DOX6 rapidly adhering to the CNT within about the first 5 ns, showing a smaller spacing. Subsequently, the distances between these DOX molecules and CNT further reduce slowly in 30–60 ns and remain almost constant in 60–80 ns, which is in line with the results exhibited in the visualization diagrams of Figure 6C–6E.

The different molecular groups in FCNT all come into contact with DOX molecules, and van der Waals forces are considered the main interaction between them

The findings in Figure 8 are designed to provide insight into the mutual contact between FCNT and the target drug DOX, where the green curve represents the atomic contacts between PAA and DOX. The increasing trend in this curve is consistent with the process of DOX gradually approaching FCNT and interacting with it as the simulation time increases, and the small change in contact number between 60 and 80 ns also proves the stability of the structure in the last 20 ns time. In an attempt to visualize the characterization of the contact between the PAA system and the DOX molecules, the conformational map at the 80 ns moment is shown in Figure 8(a$_1$). The minimum distance of atomic contact between PAA and DOX, with an average value of 0.169 nm over a time range of 60–80 ns, is labeled in the upper right corner of (a1). Correspondingly, the atomic contacts between the NIP system of FCNT and the DOX molecules are demonstrated by the yellow curve and (a2), while the contacts between the CNT system and the DOX molecules are shown by the black curve and (a3). Due to the dynamic changes in the positions of the molecules, the contact of the NIP system with the DOX molecules increases and then decreases during the first 60 ns, and then remains stable (yellow curve), whereas the contact of the CNT with the DOX (black curve) follows a similar trend
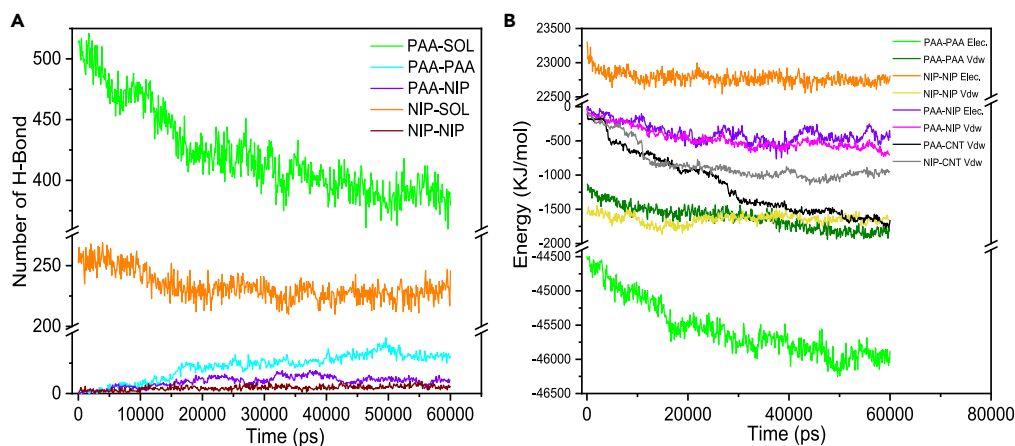
Figure 5. Hydrogen bonding and interaction forces between molecules
(A) Number of hydrogen bonds between different groups as a function of time during simulation.
(B) Elec. and Vdw. between different groups over the simulation time.

as that of PAA-DOX. These results demonstrate that DOX molecules have different degrees of contact with PAA, NIP, and CNT in FCNT during their attachment to FCNT, with relatively more interatomic contacts with PAA and NIP, and relatively minimal interatomic distances with PAA.

Figure 9A shows the number of hydrogen bonds between DOX molecules and FCNT. As shown in the figure, the aggregation of dispersed DOX molecules to FCNT causes a rapid decrease in the number of hydrogen bonds between them and water molecules (blue curve) and a slow increase in the number of hydrogen bonds between themselves (red curve). After about 30 ns, the number of hydrogen bonds between DOX molecules and PAA and NIP significantly increases, which corresponds to the time points of distance change in Figure 7, suggesting that hydrogen bonding is one of the important forms of interaction between DOX and FCNT.

Figure 9B shows the Elec. and Vdw between DOX molecules and FCNT. As shown in the figure, the magnitude of Elec. of DOX-DOX (black curve) fluctuates less while Vdw of DOX-DOX (red curve) changes drastically, suggesting that the van der Waals force is the dominant form of interaction between DOX molecules. Both Elec. (green curve) and Vdw (olive green curve) of DOX-PAA decrease significantly after about 30 ns, indicating that both van der Waals and electrostatic interactions are important driving forces for PAA to capture DOX. Similarly, the Elec. (orange curve) and Vdw (yellow curve) of DOX-NIP also significantly decreases with simulation time, and the large magnitude of the latter change indicates that van der Waals interaction is dominant during the interaction between DOX and NIP. The changes shown by the purple curve correspond to the van der Waals interactions occurring between DOX and CNT. To further investigate the interaction form between DOX and CNT, a snapshot of the orientation of DOX molecules relative to the CNT sidewall at 80 ns is extracted and displayed in Figure S2. Figure S2A demonstrates the information that the tricyclic portion of the DOX6 is aligned along the CNT tube and parallel to the tube sidewall (the other ring does not fall toward the CNT), with a spacing of 0.326 nm from the sidewall, which constitutes a typical F-type (face-to-face) π-π stacking.[13] The system consisting of DOX molecules numbered 1, 2, 4, 8, and 10 does not consider the presence of π-π stacking with CNT due to their distance up to 0.860 nm from the CNT sidewall. From Figure S2B, it can be seen that a ring (0.376 nm from tube sidewall) in DOX9 exhibits F-type π-π stacking with the CNT, and the tricyclic portion of DOX molecules numbered 2, 3, 5, and 9 are almost perpendicular to the CNT sidewall, the spacing of 0.412 nm means that they have weak T-type (edge-to-face) π-π stacking with the CNT. Discussion of Figure S2 suggests that π-π stacking is the main adhesion force for DOX attachment to CNT sidewall, which is similar to the findings reported by Karnati et al.[13–15] Overall, by comparing the energy curves in Figure 9B, the van der Waals forces are considered the main interactions between DOX and FCNT, which is consistent with the findings of Hasanzade et al.[37] who report the core conclusion that van der Waals interactions are identified as the main interactions for loading DOX using cucurbit [n] urils (n = 7, 10).

Limitations of the study

It is critical to recognize several limitations of this study. There are many adjustable variables in the initial conditions of the simulation system, including the CNT size, the chain length of PAA and NIP, the concentration of molecules, and the force field used in the simulation system, and while the probability is that these variables do not have an unpredictable impact on the core conclusions of the study, there must exist combinations of parameters that would make the results of the simulations more satisfactory, and, indeed, these variables have not been taken into account individually in this study. In addition, based on the findings that the driving force for the formation of PAA-NIP-CNT-type DDS is mainly non-covalent bonding interactions, it is easy to speculate that individual functional molecules can exhibit their drug-carrying advantages (pH, temperature, and light radiation sensitivity) due to their chemical structural integrity. However, even so, the simulation work of drug release under different excitation factors such as pH, temperature, and optical radiation is still attractive due to the possibility of many
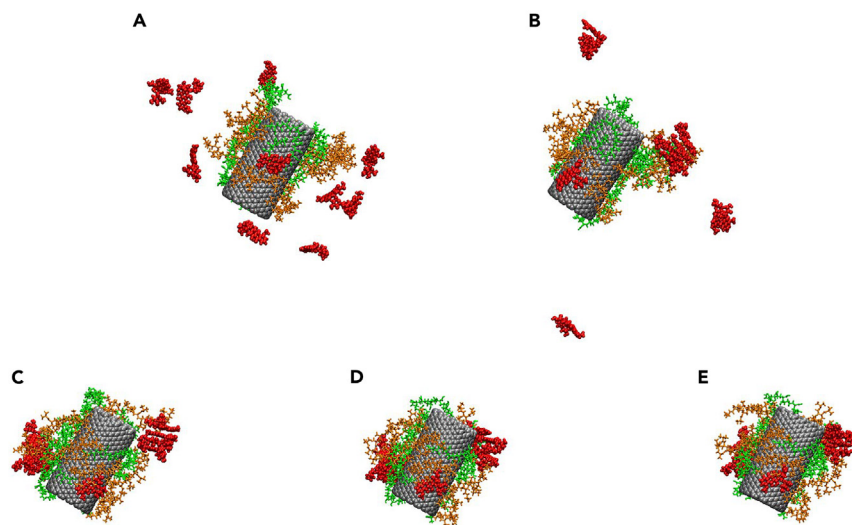
Figure 6. Snapshots taken during an 80-ns simulation of capturing drug DOXs by FCNT
(A–E) (A) 0 ns, (B) 20 ns, (C) 40 ns, (D) 60 ns, and (E) 80 ns. CNT (gray), PAAs (green), NIPs (orange) DOXs (red). For clarity, water and virtual sites are not shown.

interesting results, which are not represented in this paper. Another limitation of this work is that it does not involve experiments; experimental synthesis of the target DDS would allow the reliability of the simulation results to be assessed with the help of different assays, thus advancing the process of translating the research results into clinical applications. While our work has validated the feasibility of synthesizing the target DDS using molecular simulation techniques and has provided insight into the dynamics of such DDS formation at the molecular level, the limitations mentioned previously are indeed the ones that need to be remedied for further refinement of this work, and they will continue to be present in our subsequent research endeavors.

STAR★METHODS

Detailed methods are provided in the online version of this paper and include the following:
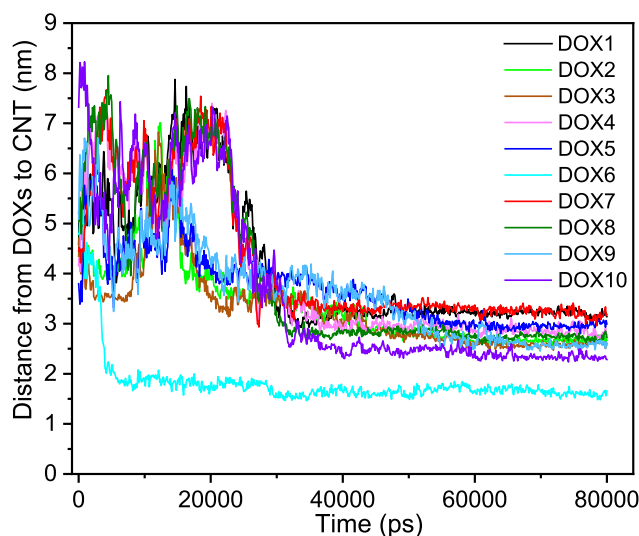
- KEY RESOURCES TABLE
- RESOURCE AVAILABILITY

Figure 7. The distance distribution between drug molecules and DDS
Distance from the center of mass of each DOX molecule (numbered 1 to 10) to the center of mass of the FCNT as a function of simulation time during the process of FCNT to catch DOXs.
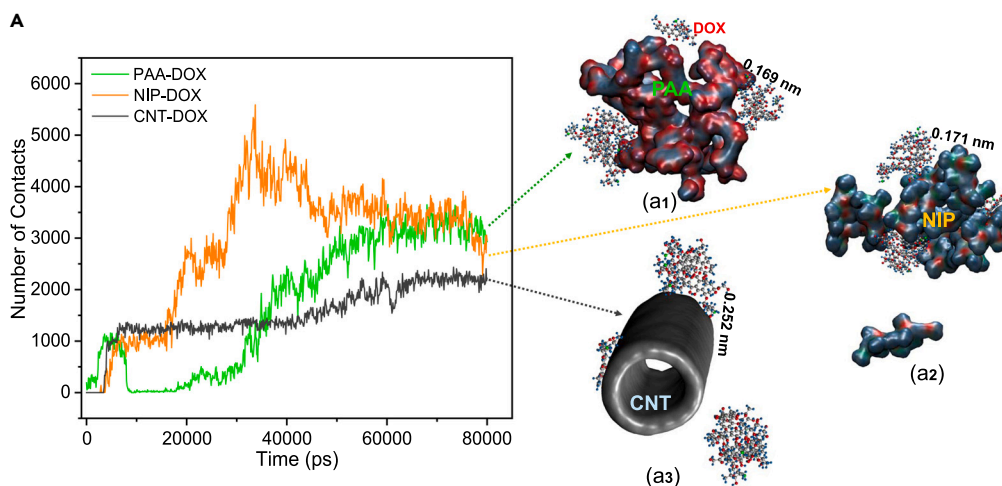
A

Figure 8. The contact distribution between drug molecules and DDS

The number of atomic contacts between the drug DOXs and the three groups of CNT, PAA, and NIP are counted and shown in (A), and the snapshots of the atomic contacts between these groups at 80 ns are shown in (a_1), (a_2), and (a_3), respectively. The values to the upper right of (a_1), (a_2), and (a_3) are the average of the minimum spacing of the atoms between the two groups during the last 20 ns (60–80 ns) of the simulation.

○ Lead contact
○ Materials availability
○ Data and code availability
● EXPERIMENTAL MODEL AND STUDY PARTICIPANT DETAILS
● METHOD DETAILS
    ○ System preparation
    ○ Simulation details
    ○ Integral algorithm for motion equations
● QUANTIFICATION AND STATISTICAL ANALYSIS
● ADDITIONAL RESOURCES

SUPPLEMENTAL INFORMATION

Supplemental information can be found online at https://doi.org/10.1016/j.isci.2024.108812.
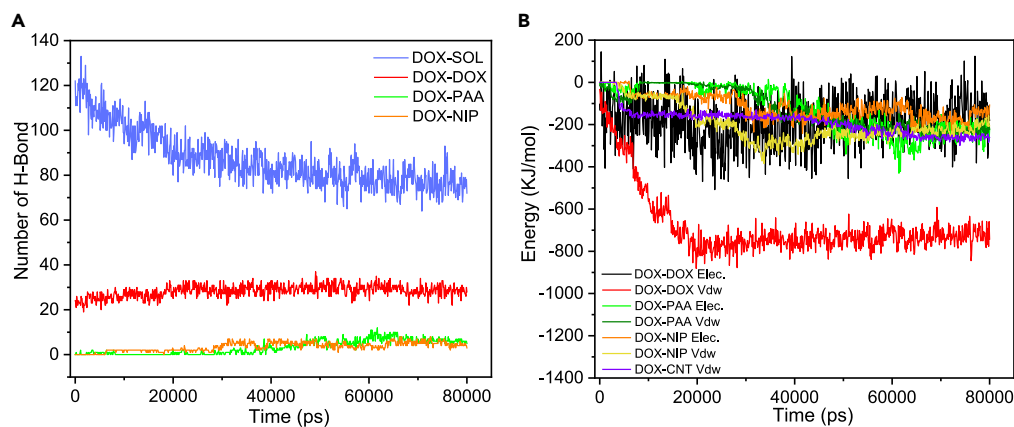

Figure 9. The interaction between drug molecules and DDS

(A) Number of hydrogen bonds between FCNT (CNT, PAA, NIP), SOL, and DOXs.

(B) Elec. and Vdw between different groups during the simulation for catching DOXs using FCNT. See also Figure S2.

ACKNOWLEDGMENTS

AUTHOR CONTRIBUTIONS

Conceptualization, Q.S.; methodology, Q.S. and Z.D.; validation, W.W.; formal analysis, P.H.; investigation, Q.S., P.H., and Z.D.; data curation, P.H. and Z.D.; writing – original draft, Q.S; writing – review & editing, Q.S. and W.W.; supervision, Q.S. and W.W.; funding acquisition, W.W.

DECLARATION OF INTERESTS

The authors declare no competing interests.

REFERENCES

1. Safari Yazd, H., Yang, Y., Li, L., Yang, L., Li, X., Pan, X., Chen, Z., Jiang, J., Cui, C., and Tan, W. (2020). Precise Deposition of Polydopamine on Cancer Cell Membrane as Artificial Receptor for Targeted Drug Delivery. iScience 23, 101750.

2. Song, X., Fu, W., and Cheang, U.K. (2022). Immunomodulation and delivery of macrophages using nano-smooth drug-loaded magnetic microrobots for dual targeting cancer therapy. iScience 25, 104507.

3. Raj, S., Khurana, S., Choudhari, R., Kesari, K.K., Kamal, M.A., Garg, N., Ruokolainen, J., Das, B.C., and Kumar, D. (2021). Specific targeting cancer cells with nanoparticles and drug delivery in cancer therapy. Semin. Cancer Biol. 69, 166–177.

4. Guerrero-Garzón, J.F., Madland, E., Zehl, M., Singh, M., Rezaei, S., Aachmann, F.L., Courtade, G., Urban, E., Rückert, C., Busche, T., et al. (2020). Class IV Lasso Peptides Synergistically Induce Proliferation of Cancer Cells and Sensitize Them to Doxorubicin. iScience 23, 101785.

5. Carroll, B.L., Bonica, J., Shamseddine, A.A., Hannun, Y.A., and Obeid, L.M. (2018). A role for caspase-2 in sphingosine kinase 1 proteolysis in response to doxorubicin in breast cancer cells-implications for the CHK1-suppressed pathway. FEBS Open Bio. 8, 27–40.

6. Chan, C., Du, S., Dong, Y., and Cheng, X. (2021). Computational and experimental approaches to investigate lipid nanoparticles as drug and gene delivery systems. Curr. Top. Med. Chem. 21, 92–114.

7. Lotfi, M., Morsali, A., and Bozorgmehr, M.R. (2018). Comprehensive quantum chemical insight into the mechanistic understanding of the surface functionalization of carbon nanotube as a nanocarrier with cladribine anticancer drug. Appl. Surf. Sci. 462, 720–729.

8. Khorram, R., Raissi, H., and Morsali, A. (2017). Assessment of solvent effects on the interaction of Carmustine drug with the pristine and COOH-functionalized single-walled carbon nanotubes: A DFT perspective. J. Mol. Liq. 240, 87–97.

9. Arabian, T., Amjad-Iranagh, S., and Halladj, R. (2021). Molecular dynamics simulation study of doxorubicin adsorption on functionalized carbon nanotubes with folic acid and tryptophan. Sci. Rep. 11, 24210.

10. Comparetti, E.J., Pedrosa, V.d.A., and Kaneno, R. (2018). Carbon nanotube as a tool for fighting cancer. Bioconjugate Chem. 29, 709–718.

11. Wei, C., Dong, X., Zhang, Y., Liang, J., Yang, A., Zhu, D., Liu, T., Kong, D., and Lv, F. (2018). Simultaneous fluorescence imaging monitoring of the programmed release of dual drugs from a hydrogel-carbon nanotube delivery system. Sensor. Actuator. B Chem. 273, 264–275.

12. Maleki, R., Afrouzi, H.H., Hosseini, M., Toghraie, D., and Rostami, S. (2020). Molecular dynamics simulation of Doxorubicin loading with N-isopropyl acrylamide carbon nanotube in a drug delivery system. Comput. Methods Progr. Biomed. 184, 105303.

13. Karnati, K.R., and Wang, Y. (2018). Understanding the co-loading and releasing of doxorubicin and paclitaxel using chitosan functionalized single-walled carbon nanotubes by molecular dynamics simulations. Phys. Chem. Chem. Phys. 20, 9389–9400.

14. Wolski, P., Nieszporek, K., and Panczyk, T. (2017). Pegylated and folic acid functionalized carbon nanotubes as pH controlled carriers of doxorubicin. Molecular dynamics analysis of the stability and drug release mechanism. Phys. Chem. Chem. Phys. 19, 9300–9312.

15. Kordzadeh, A., Amjad-Iranagh, S., Zarif, M., and Modarress, H. (2019). Adsorption and encapsulation of the drug doxorubicin on covalent functionalized carbon nanotubes: A scrutinized study by using molecular dynamics simulation and quantum mechanics calculation. J. Mol. Graph. Model. 88, 11–22.

16. Jha, R., Singh, A., Sharma, P.K., and Fuloria, N.K. (2020). Smart carbon nanotubes for drug delivery system: A comprehensive study. J. Drug Deliv. Sci. Technol. 58, 101811.

17. Al-Qattan, M.N., Deb, P.K., and Tekade, R.K. (2018). Molecular dynamics simulation strategies for designing carbon-nanotube-based targeted drug delivery. Drug Discov. Today 23, 235–250.

18. Yaghoubi, A., and Ramazani, A. (2020). Anticancer DOX delivery system based on CNTs: Functionalization, targeting and novel technologies. J. Contr. Release 327, 198–224.

19. Kavyani, S., Dadvar, M., Modarress, H., and Amjad-Iranagh, S. (2018). Molecular Perspective Mechanism for Drug Loading on Carbon Nanotube-Dendrimer: A Coarse-Grained Molecular Dynamics Study. J. Phys. Chem. B 122, 7956–7969.

20. Dubey, R., Dutta, D., Sarkar, A., and Chattopadhyay, P. (2021). Functionalized carbon nanotubes: Synthesis, properties and applications in water purification, drug delivery, and material and biomedical sciences. Nanoscale Adv. 3, 5722–5744.

21. Huang, Y.P., Lin, I.J., Chen, C.C., Hsu, Y.C., Chang, C.C., and Lee, M.J. (2013). Delivery of small interfering RNAs in human cervical cancer cells by polyethylenimine-functionalized carbon nanotubes. Nanoscale Res. Lett. 8, 267.

22. Taghavi, S., Nia, A.H., Abnous, K., and Ramezani, M. (2017). Polyethylenimine-functionalized carbon nanotubes tagged with AS1411 aptamer for combination gene and drug delivery into human gastric cancer cells. Int. J. Pharm. 516, 301–312.

23. Rezaian, M., Maleki, R., Dahri Dahroud, M., Alamdari, A., and Alimohammadi, M. (2018). pH-Sensitive Co-Adsorption/Release of Doxorubicin and Paclitaxel by Carbon Nanotube, Fullerene, and Graphene Oxide in Combination with N-isopropylacrylamide: A Molecular Dynamics Study. Biomolecules 8, 127–135.

24. Kamath, A., Laha, A., Pandiyan, S., Aswath, S., Vatti, A.K., and Dey, P. (2022). Atomistic investigations of polymer-doxorubicin-CNT compatibility for targeted cancer

treatment: A molecular dynamics study. J. Mol. Liq. *348*, 118005.

25. Farokh, A., Pourmadadi, M., Rashedi, H., Yazdian, F., and Navaei-Nigjeh, M. (2023). Assessment of synthesized chitosan/halloysite nanocarrier modified by carbon nanotube for pH-sensitive delivery of curcumin to cancerous media. Int. J. Biol. Macromol. *237*, 123937.

26. Kordzadeh, A., Zarif, M., and Amjad-Iranagh, S. (2023). Molecular dynamics insight of interaction between the functionalized-carbon nanotube and cancerous cell membrane in doxorubicin delivery. Comput. Methods Progr. Biomed. *230*, 107332.

27. Li, H.J., Li, P.Y., Li, L.Y., Haleem, A., and He, W.D. (2018). Gold Nanoparticles Grafted with PLL-b-PNIPAM: Interplay on Thermal/pH Dual-Response and Optical Properties. Molecules *23*, 921.

28. Zhao, J., Zhang, Z., and Wang, X. (2020). Fabrication of pH-responsive PAA-NaMnF3@DOX hybrid nanostructures for magnetic resonance imaging and drug delivery. J. Alloys Compd. *820*, 153142.

29. Dai, Z., Shu, Y., Wan, C., and Wu, C. (2016). Effects of Culture Substrate Made of Poly(N-isopropylacrylamide-co-acrylic acid) Microgels on Osteogenic Differentiation of Mesenchymal Stem Cells. Molecules *21*, 1192.

30. Kamaraj, S., Palanisamy, U.M., Kadhar Mohamed, M.S.B., Gangasalam, A., Maria, G.A., and Kandasamy, R. (2018). Curcumin drug delivery by vanillin-chitosan coated with calcium ferrite hybrid nanoparticles as carrier. Eur. J. Pharmaceut. Sci. *116*, 48–60.

31. Zhu, Y., Wang, J., Vanga, S.K., and Raghavan, V. (2021). Visualizing structural changes of egg avidin to thermal and electric field stresses by molecular dynamics simulation. Lebensm. Wiss. Technol. *151*, 112139.

32. Chen, H., and Panagiotopoulos, A.Z. (2019). Molecular Modeling of Surfactant Micellization Using Solvent-Accessible Surface Area. Langmuir *35*, 2443–2450.

33. Sica, M.P., Kortsarz, M.V., Morillas, A.A., and Smulski, C.R. (2022). Protocol to study the oligomeric organization of single-span transmembrane peptides using molecular dynamics simulations. STAR Protoc. *3*, 101636.

34. Dai, X., Chen, L., Liao, Y., Sheng, M., Qu, Q., Shi, Y., and Shi, X. (2022). Formulation design and mechanism study of hydrogel based on computational pharmaceutics theories. J. Mol. Graph. Model. *110*, 108051.

35. Abdulkareem, U., Kartha, T.R., and Madhurima, V. (2023). Radial distribution and hydrogen bonded network graphs of alcohol-aniline binary mixture. J. Mol. Model. *29*, 151.

36. Zhao, Q., Gao, H., Su, Y., Huang, T., Lu, J., Yu, H., and Ouyang, D. (2019). Experimental characterization and molecular dynamic simulation of Ketoprofen-Cyclodextrin complexes. Chem. Phys. Lett. *736*, 136802.

37. Hasanzade, Z., and Raissi, H. (2020). Molecular mechanism for the encapsulation of the Doxorubicin in the cucurbit [n] urils cavity and the effects of diameter, protonation on loading and releasing of the anticancer drug: Mixed quantum mechanical/molecular dynamics simulations. Comput. Methods Progr. Biomed. *196*, 105563.

38. Kim, S., Chen, J., Cheng, T., Gindulyte, A., He, J., He, S., Li, Q., Shoemaker, B.A., Thiessen, P.A., Yu, B., et al. (2023). PubChem 2023 update. Nucleic Acids Res. *51*, D1373–D1380.

39. Dennington, R., Keith, T.A., and Millam, J.M. (2016). GaussView, version 6.0.16 (Semichem Inc). https://gaussian.com/gaussview6/.

40. Frisch, M.J., Trucks, G.W., Schlegel, H.B., Cheeseman, J., Scalmani, G., Marenich, A., Zheng, J., Clemente, F., Zou, L., et al. (2016). Gaussian 16, Revision C.01. https://gaussian.com/gaussian16/.

41. Humphrey, W., Dalke, A., and Schulten, K. (1996). VMD: Visual molecular dynamics. J. Mol. Graph. *14*, 33.

42. Lu, T., and Chen, F. (2012). Multiwfn: A multifunctional wavefunction analyzer. J. Comput. Chem. *33*, 580–592.

43. Lu, T.. Sobtop, Version 1.0(dev3.1). http://sobereva.com/soft/Sobtop.

44. Van Der Spoel, D., Lindahl, E., Hess, B., Groenhof, G., Mark, A.E., and Berendsen, H.J.C. (2005). GROMACS: fast, flexible, and free. J. Comput. Chem. *26*, 1701–1718.

45. Smith, T.J., and Stevenson, K.J. (2004). Origin 7.5 OriginLab Corporation, One Roundhouse Plaza, Northampton, MA 01060. 1-800-969-7720. price $699.00 (retail,singleuser), $489.00 (educational, single user). Contact company for other pricing options. J. Am. Chem. Soc. *126*, 6834.

46. Becke, A.D. (1993). Density-functional thermochemistry. III. The role of exact exchange. J. Chem. Phys. *98*, 5648–5652.

47. Schauperl, M., Nerenberg, P.S., Jang, H., Wang, L.P., Bayly, C.I., Mobley, D.L., and Gilson, M.K. (2020). Non-bonded force field model with advanced restrained electrostatic potential charges (RESP2). Commun. Chem. *3*, 44.

48. Zhang, J., and Lu, T. (2021). Efficient evaluation of electrostatic potential with computerized optimized code. Phys. Chem. Chem. Phys. *23*, 20323–20328.

49. Ke, Q., Gong, X., Liao, S., Duan, C., and Li, L. (2022). Effects of thermostats/barostats on physical properties of liquids by molecular dynamics simulations. J. Mol. Liq. *365*, 120116.

STAR★METHODS

KEY RESOURCES TABLE

REAGENT or RESOURCE	SOURCE	IDENTIFIER
Deposited data		
The structure data of the simulation system	This paper; Mendeley Data	https://doi.org/10.17632/bjpfs3ybt3.1
Data on the relative positions and interactions between different groups in a simulation system	This paper; Mendeley Data	https://doi.org/10.17632/bjpfs3ybt3.1
Software and algorithms		
PubChem website	National Institutes of Health (NIH); Kim et al.[38]	https://pubchem.ncbi.nlm.nih.gov/
GaussView version 6.0	Dennington et al.[39]	https://gaussian.com/gaussview6/
Gaussian version 16	Frish et al.[40]	https://gaussian.com/gaussian16/
VMD version 1.9.3	Humphrey et al.[41]	https://www.ks.uiuc.edu/Research/vmd/
Multiwfn version 3.8 (dev)	Lu et al.[42]	http://sobereva.com/multiwfn/
Sobtop version 1.0 (dev3.1)	Lu et al.[43]	http://sobereva.com/soft/Sobtop
GROMACS version 2022.1	Spoel et al.[44]	https://manual.gromacs.org/
Origin version 2019b	OriginLab Corporation; Smith et al.[45]	https://www.originlab.com/
GROMACS commands used to extract the simulation data	This paper; Mendeley Data	https://doi.org/10.17632/bjpfs3ybt3.1

RESOURCE AVAILABILITY

Lead contact

Further information and requests for resources and reagents should be directed to and will be fulfilled by the lead contact, Qijiang Shu (14787485422@163.com).

Materials availability

This study did not generate new unique reagents.

Data and code availability

- All original data of visual figures reported in this paper have been deposited at Mendeley Data and are publicly available as of the date of publication. The DOI is listed in the key resources table.
- This paper does not report original code.
- Any additional information required to reanalyze the data reported in this paper is available from the lead contact upon request.

EXPERIMENTAL MODEL AND STUDY PARTICIPANT DETAILS

Our study does not use experimental models typical in the life sciences, it is computational simulation research.

METHOD DETAILS

System preparation

A single-walled CNT with a diameter of 20.31 Å, a length of 40.00 Å, and a chiral vector of (m = 15, n = 15) are generated using VMD software.[41] The chemical structures of DOX, PAA, and NIP are obtained from the PubChem website,[38] followed by the construction of a 20-mer molecule of PAA and a 10-mer molecule of NIP using GaussView software,[39] respectively. Structural optimization of DOX, PAA, and NIP is carried out using Gaussian software by invoking its integrated DFT, B3LYP/6-311G** calculations,[40,46] the RESP charges[47] of these molecules are fitted with the help of Multiwfn software,[42,48] and subsequently, top files of these molecules under the GAFF force field are generated with Sobtop software.[43] The chemical structures and corresponding charges of DOX, PAA, and NIP are shown in Figure S3.

Simulation details

A cubic simulation box with a size of 10 × 10 × 10 nm^3 is constructed with a CNT inserted in the center and ten 20-mer PAA molecules and ten 10-mer NIP molecules inserted at random positions, respectively, followed by the solvation treatment of the system, TIP4P water model is

applied as solvent. Energy minimization simulation is run, followed by coupling the system to 300 K using the V-rescale algorithm[49] and 100 ps simulation time to obtain an NVT ensemble, then controlling the system pressure to stabilize it at 1.0 bar utilizing the Berendsen algorithm[49] and 100 ps simulation time to obtain an NPT ensemble, and finally simulating 60 ns to produce a functionalized CNT (FCNT). Ten DOX molecules are randomly inserted in a $10 \times 10 \times 10$ nm^3 simulation box with an FCNT placed in the center, equilibrium simulations corresponding to the energy minimization, NVT ensemble, and NPT ensemble described previously are successively run on such a system, followed by an 80 ns simulation to produce a finished system of FCNT loading DOX. All simulations are performed with a time step of 2 fs using the GROMACS software package.[44] During the simulation, bonds involving hydrogen atoms are converted to constraints using the LINCS algorithm,[44] the electrostatic interactions are calculated using the particle mesh Ewald method, and the cut-off radii of both electrostatic and Lennard-Jones interactions are taken as 1.2 nm. Molecular visualizations are generated using the VMD software package.[41]

Integral algorithm for motion equations

The initial step of the simulation is to run an energy minimization to eliminate possible excessive repulsive forces in the system, which is mathematically equivalent to the problem of going to the extremes of a multivariate function of the force, which can be expressed as：

$$F_A = -\frac{\partial E(R_1, R_2, \ldots, R_N)}{\partial R_A} = 0 \quad A = 1, 2, \ldots, N \quad \text{(Equation 3)}$$

where F denotes the force on the atom and R denotes the position vector of the atom. In our simulations, the steepest descent method is used to obtain the solution of the equation.

The core purpose of MD simulation is to obtain the relationship between the position coordinate R and velocity V of atoms over time t. In the simulation of the NVT ensemble, NPT ensemble, and finished product of this paper, the Leap-frog algorithm[44] is used to obtain all R (t) and V (t). This algorithm can be expressed as the following set of equations:

$$R(t + \Delta t) = R(t) + V\left(t + \frac{1}{2}\Delta t\right)\Delta t \quad \text{(Equation 4)}$$

$$V\left(t + \frac{1}{2}\Delta t\right) = V\left(t - \frac{1}{2}\Delta t\right) + a(t)\Delta t \quad \text{(Equation 5)}$$

$$V(t) = \frac{1}{2}\left[V\left(t + \frac{1}{2}\Delta t\right) + V\left(t - \frac{1}{2}\Delta t\right)\right] \quad \text{(Equation 6)}$$

where Δt is step width. The combination of Equations 4, 5, and 6 allows for iterative computations to complete the numerical integration of Newton's equations of motion from t = 0 up to a specified upper time limit.

QUANTIFICATION AND STATISTICAL ANALYSIS

The gmx gyrate command in GROMACS software is used to calculate the evolution of the radius of gyration of the components of interest in the system over time. The obtained data are plotted as visualization curves by Origin software,[45] as shown in Figure 2A in this paper. Similarly, the gmx sasa command is employed to calculate the solvent accessible surface area of the group of interest in the system, with the radius of the solvent probe being defaulted to 0.14 nm in the program, and these data are similarly plotted as shown in Figure 2B in this paper. The gmx distance command is used to statistically analyze the changes in the distance between the centroids of different components (residues) in the system. The plotted curves are shown in Figures 3 and 7 of this paper. The gmx mindist command is used to count the number of contacts between atoms of interest in the system. When calculating, the program defines the distance between atoms less than 0.6 nm as mutual contact. Their visualized curves can be seen in Figures 4 and 8 of this paper. The gmx mindist command can also be used to calculate the minimum distance between atoms between groups over time and provide the average of these minimum distances, as shown in Figure 8 of this paper. The radial distribution function between the different groups in the system is calculated using the gmx rdf command and is plotted as shown in Figure 4B in this paper. The number of hydrogen bonds in the system is counted with the gmx hbond command. In the program, hydrogen bonding is determined based on a combination of the cutoff value for the angle made by the hydrogen-donor-acceptor and the cutoff value for the distance between the donor-acceptor. The OH and NH groups are used as donors, O is always used as the acceptor, and N is the acceptor by default. The program defaults to an angle cutoff value of 30° and a distance cutoff value of 0.35 nm when counting. The curves plotted with the number of hydrogen bonds being counted can be seen in Figures 5A and 9A of this paper. The interaction energy between the components of interest in the system can be calculated using the gmx energy command, and the extracted data are plotted as curves as shown in Figures 5B and 9B of this paper.

ADDITIONAL RESOURCES

Our study has not generated or contributed to a new website/forum, and it is not part of a clinical trial.